# Supercapacitors Based on Graphene-Supported Iron Nanosheets as Negative Electrode Materials

**Conglai Long, Tong Wei, Jun Yan, Lili Jiang, and Zhuangjun Fan***

Key Laboratory of Superlight Materials and Surface Technology, Ministry of Education, College of Material Science and Chemical Engineering, Harbin Engineering University, Harbin 150001, China

**ABSTRACT** We report a facile strategy to prepare iron nanosheets directly grown on graphene sheets nanocomposite (C-PGF) through the carbonization of iron ions adsorbed onto polyaniline nanosheet/graphene oxide hybrid material. Because of the synergistic effect of iron nanosheets and graphene sheets, the as-obtained C-PGF exhibits an ultrahigh capacitance of *ca.* 720 F $g^{-1}$ in 6 M KOH aqueous solution. Additionally, the assembled asymmetric supercapacitor (C-PGF//$Ni(OH)_2$/CNTs) delivers a remarkable high power density and a noticeable ultrahigh energy density of *ca.* 140 Wh $kg^{-1}$ (based on the total mass of active materials) and an acceptable cycling performance of 78% retention after 2000 cycles. Therefore, the designed supercapacitors with high energy density, comparable to rechargeable lithium-ion batteries (LIBs), offer an important guideline for future design of advanced next-generation supercapacitors for both industrial and consumer applications.

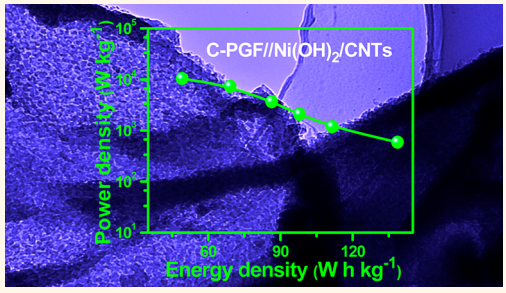


**KEYWORDS:** supercapacitors · graphene · iron nanosheets · ultrahigh energy density

Supercapacitors (also known as ultracapacitors or electrochemical capacitors), with a higher power density than lithium-ion batteries (LIBs), are of great interest for their potential applications in portable electronics, back-up power devices, hybrid electronic vehicles.[1−5] However, the low energy density of supercapacitors (usually less than 10 Wh $kg^{-1}$) greatly limits their further application.[1,4] Therefore, the improvement of energy density of supercapacitors without sacrificing their high power capability to be close to or even beyond that of batteries remains a big challenge.[6−9]

Recently, asymmetric (hybrid) systems have been extensively explored by combining complementary potential windows of the positive electrode and negative electrode to increase the operation voltage, resulting in a notable improvement of the energy density.[10] Traditionally, the positive materials with the working potential window above 0 V (*vs* NHE) mainly consist of $RuO_2$, $MnO_2$, $V_2O_5$, $PbO_2$, $Co_3O_4$, $Ni(OH)_2$ and conductive polymer, which show ultrahigh capacitance normally higher than 700 F $g^{-1}$.[8,11−15] With regard to the negative materials, carbonaceous materials such as porous carbons,[16−18] carbon nanotubes (CNTs),[19,20] graphene[21−23] often act as electrodes with the working potential window below 0 V (*vs* NHE) for asymmetric supercapacitors; however, their specific capacitances are less than 300 F $g^{-1}$ in aqueous electrolyte.[24] From the foregoing, the unbalance of specific capacitance between the positive materials and the negative materials limits the improvement of the energy density for supercapacitors. In order to address this problem, it is urgent to develop a new negative material with a high specific capacitance and a good rate performance.

Iron-based materials have been receiving considerable attention due to their low cost, abundance in nature and being environmentally benign. Additionally, iron oxides (including hydroxides) have been widely investigated as the negative electrode materials for supercapacitor.[25,26] However, iron oxide ($FeO_x$) electrodes still show a relatively low capacitance (<300 F $g^{-1}$) in aqueous electrolyte,[27−29] limiting from their low diffusion coefficient for electron transfer. As known, the incorporation $FeO_x$ nanoparticles

* Address correspondence to fanzhj666@163.com.

Received for review October 5, 2013 and accepted November 12, 2013.

**Published online November 12, 2013**
**10.1021/nn405192s**

© 2013 American Chemical Society

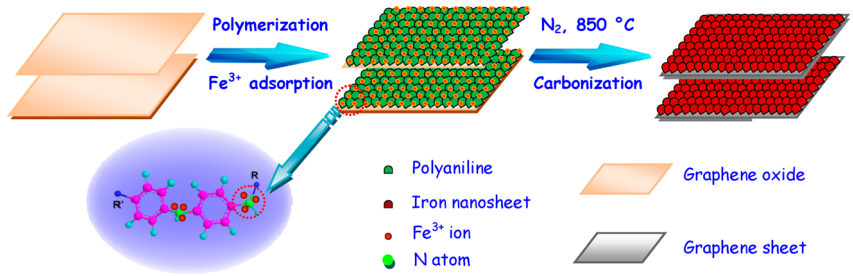


**Scheme 1. Schematic illustration of the formation of iron nanocomposite with fish scale-like iron nanosheets supported on graphene sheets.**

into carbonaceous materials (such as CNTs, carbon black and carbon fibers) can significantly enhance their electrochemical performance.[25,26,30] Recently, $FeO_x$ coupled with graphene sheets has shown an expected capacitance, and a high energy density for hybrid supercapacitors as a negative material.[25,31] Thus, the design of iron oxide−carbon hybrid material with strongly coupled structure is important for achieving high performance supercapacitors.

Herein, we report a facile strategy to prepare fish scale-like iron nanosheets arrayed on graphene sheets nanocomposite (C-PGF) by the carbonization of $Fe^{3+}$ adsorbed onto polyaniline (PANI) nanosheets/graphene oxide (GO) hybrid material, as shown in Scheme 1.

Benefiting from the full use of pseudocapacitance of iron-based active materials that highly coupled on the nitrogen-doped conductive graphene sheets, as well as fast electron/ion transport in the electrodes, the as-obtained C-PGF exhibits an ultrahigh capacitance of 720 F $g^{-1}$. More importantly, the assembled asymmetric supercapacitor (C-PGF//$Ni(OH)_2$/CNTs) using $Ni(OH)_2$/CNTs as a positive electrode and iron nanocomposite as a negative electrode, delivers a remarkable high power density and a noticeable ultrahigh energy density of *ca.* 140 Wh $kg^{-1}$ (based on the total mass of active materials), much higher than other asymmetric supercapacitors,[9,32−35] and comparable to rechargeable LIBs.[36,37]

## RESULTS AND DISCUSSION

2D fish scale-like PANI arrayed on GO (Figure 1a) was prepared by template-free *in situ* polymerization method. After the carbonization, pyrolytic carbon nanosheets (C-PG) still maintain their original morphology on the graphene sheets (Figure 1b). More interestingly, $Fe^{3+}$ cations could easily adsorb onto PANI/GO (PG) composite by the complexation and electrostatic interactions due to the existence in enormous binding sites like nitrogen and oxygen-containing functional groups on PANI and GO,[38,39] as proved by FTIR (Figure S1, Supporting Information), and its saturated adsorption amount is up to 225 mg $g^{-1}$ (Figure S2, Supporting Information). During the pyrolysis process, $Fe^{3+}$ could be *in situ* reduced to metallic iron (α-Fe, JCDPS No. 06−0696) by the reaction with pyrolytic carbon from PANI, and there is a small amount of orthorhombic $Fe_3C$ due to the partial dissolution of carbon atoms into Fe crystal lattices at elevated temperature,[40,41] as confirmed by X-ray diffraction (XRD) analysis (Figure 2a). Moreover, there is a broad and weak diffraction peak around 25° that can be assigned to the reflections of graphitic plane (002), indicating a graphitization of carbon material. X-ray photoelectron spectroscopy (XPS) analysis reveals 3 wt % nitrogen content in the hybrid material, and *ca.* 45.7 wt % carbon is calculated by thermal gravimetric (TG) analysis (Figure S3, Supporting Information). Additionally, the intensity ratio of D band and G band ($I_D/I_G$) for C-PGF is about 0.88, implying good graphitization degree (Figure S4, Supporting Information). Transmission electron microscopy (TEM) image (Figure 1c) shows that as-obtained hybrid material presents a fish scale-like structure with sizes of 10−20 nm.

The high-resolution TEM (HRTEM) image (Figure 1d) reveals that the interplane spacing is *ca.* 0.2 nm, which is indexed to (110) of iron nanosheets. Additionally, iron nanosheets strongly couple with graphene sheets (marked by arrow in Figure 1d). Also selected area electron diffraction (SAED) pattern (inset of Figure 1d) confirms the presence of the quasi-single-crystalline iron. For comparison, there are aggregated particles containing iron and iron oxide using other carbon precursors such as PANI and GO (Figure S5, Supporting Information), confirming that the template PANI nanosheets could direct the formation of iron nanosheets during the carbonization process. Furthermore, the scanning transmission electron microscopy (STEM) of C-PGF (Figure 1e) reveals the nanocomposite possesses nanostructure consisting of iron nanosheets supported on nitrogen-doped graphene sheets. The elemental mappings (Figure 1f, g, h) demonstrate the uniform distribution of carbon and iron, as well as the doping of nitrogen.

The nitrogen adsorption and desorption isotherm and the pore-size-distribution (PSD) curves (Figure 2b) exhibit that it exists mesoporous structure for C-PG and C-PGF. Moreover, the similar pore size distribution of the carbonized PANI/GO hybrid material with/without $Fe^{3+}$ doping further confirms the template effect. Notably,

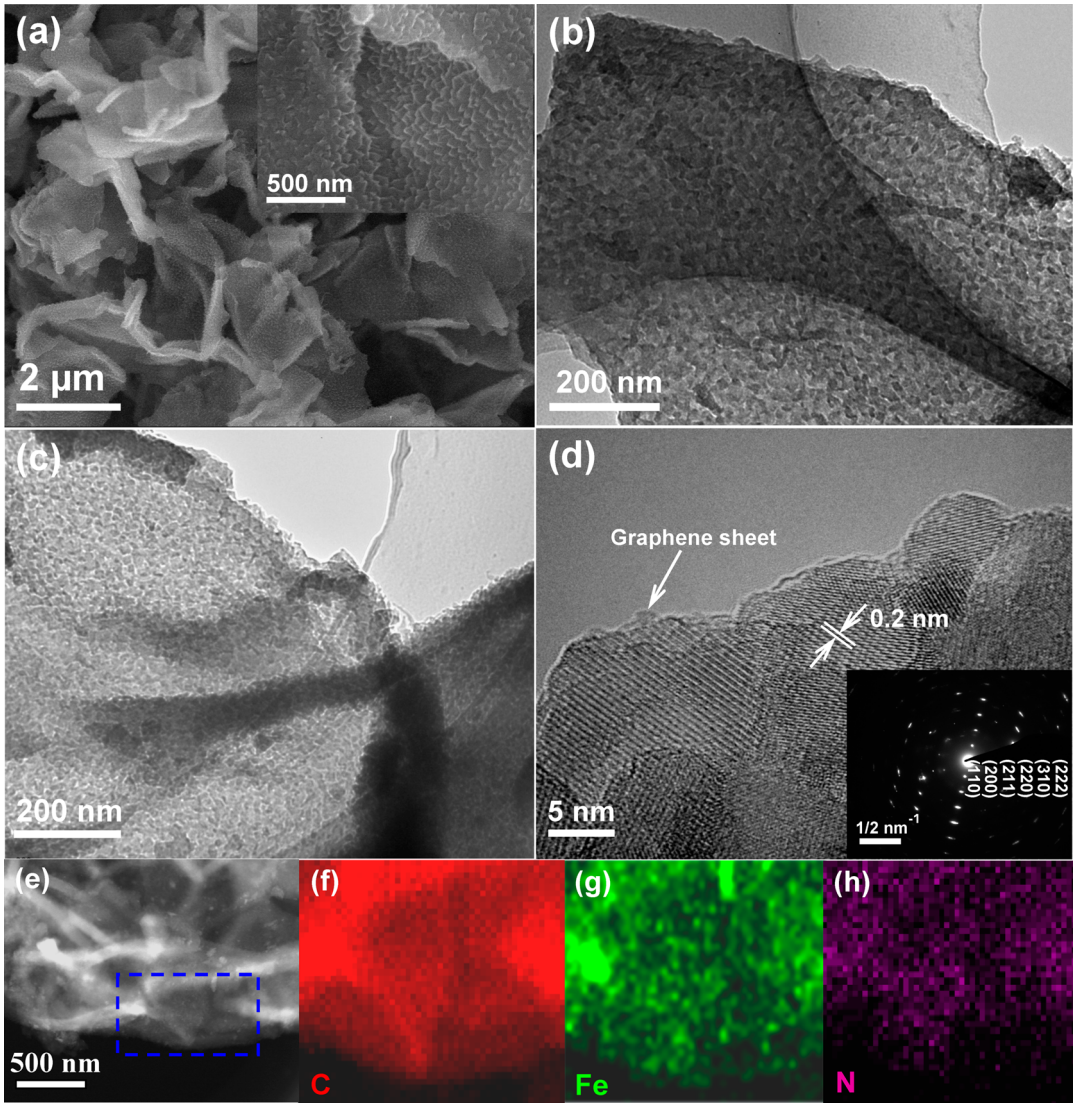


Figure 1. (a) SEM images with different magnifications of polyaniline/graphene oxide (PG). (b) TEM image of C-PG. (c) TEM image of the typical iron nanocomposite (C-PGF) with iron nanosheets arrayed on graphene sheets. (d) HRTEM image of C-PGF and the SAED patterns (inset) of iron nanosheets. (e) Typical STEM image of C-PGF. Corresponding elemental mapping images of C (f), Fe (g), and N (h) in the bule square region of (e).

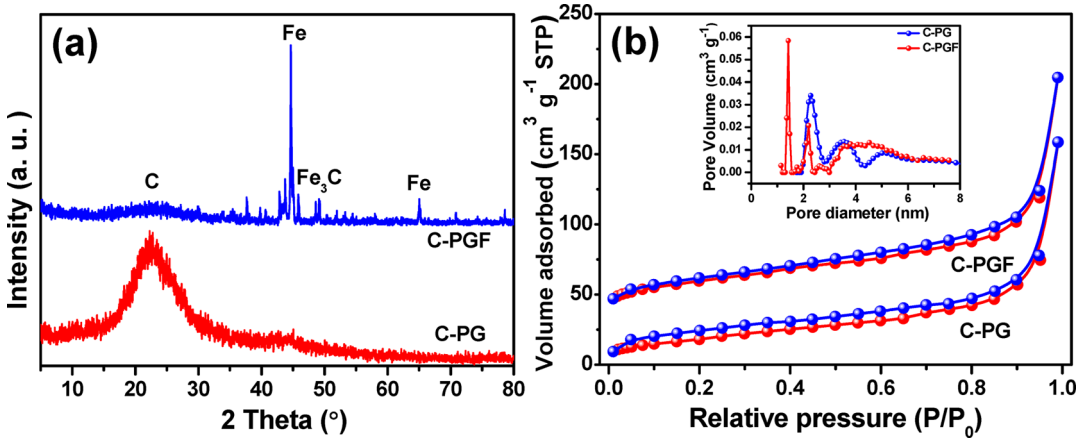


Figure 2. (a) XRD patterns of C-PGF and C-PG. (b) Typical nitrogen adsorption/desorption isotherms and pore-size-distribution (PSD) curves (inset) of the C-PGF and C-PG.

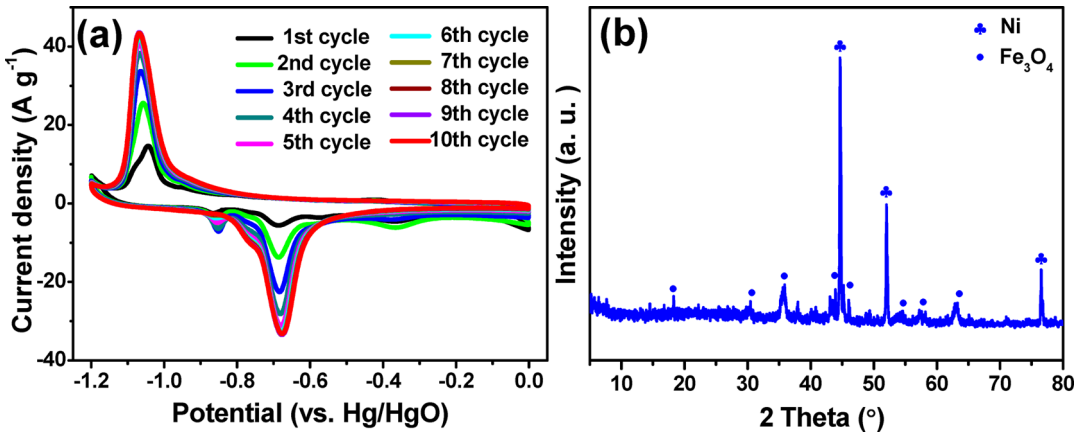


**Figure 3. (a) The CV curves of initial 10 cycles for C-PGF in 6 M KOH solution at a scan rate of 10 mV $s^{-1}$. (b) XRD pattern of C-PGF at the end of charge (0 V *vs* Hg/HgO).**

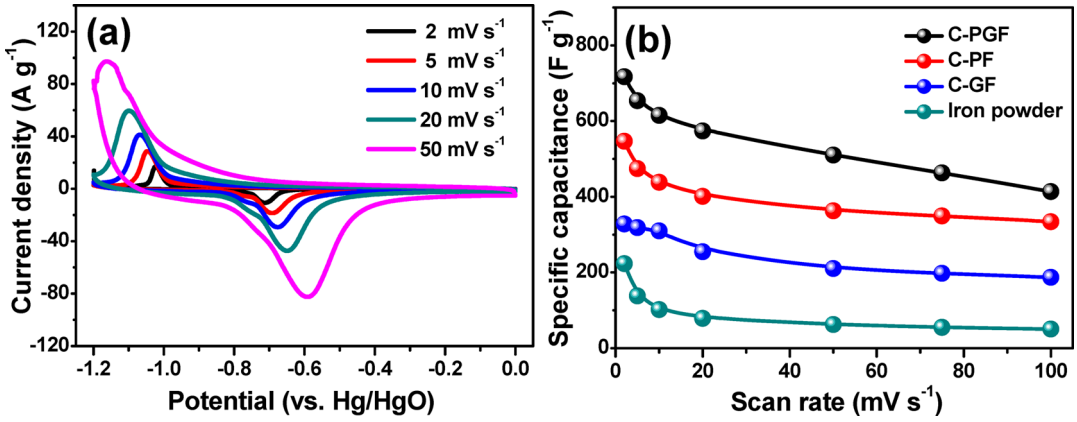


**Figure 4. (a) The CV curves of C-PGF at various scan rates in 6 M KOH solution. (b) The specific capacitance of C-PGF, C-PF, C-GF and iron powder electrode at various scan rates.**

there is an additional micropore centered at 1.4 nm for C-PGF, which maybe comes from the reaction of carbon and iron at elevated temperature, resulting in higher surface area (218 $m^2$ $g^{-1}$) than that of C-PG (70 $m^2$ $g^{-1}$) (also see Table S1, Supporting Information). Therefore, this sheet−sheet structure with high specific surface area and plentiful mesopores is favorable for improving both the pseudocapacitance of iron nanosheets and the electric double-layer (EDL) capacitance of graphene, since the hydrated ions in the electrolyte are easily accessible to the exterior and interior pore surfaces that would be beneficial to redox reaction for application in supercapacitors.

As an electrode for supercapacitors, cyclic voltammogram (CV) curves of C-PGF (Figure 3a) exhibit the enhanced current density with increasing of cycle number until the seventh cycle, suggesting an electrochemical transformation from Fe to $Fe_3O_4$ under alkaline condition, as proved by XRD analysis (Figure 3b). Notably, a couple of well-defined redox peaks (anodic peak at −0.68 V, with corresponding cathodic peak at −1.06 V) can be observed, corresponding to the reversible conversion between $Fe^{2+}$ and $Fe^{3+}$. Additionally, the other two anodic peaks (at −0.85 and −0.36 V) can be attributed to the oxidations: Fe → $Fe^{2+}$ and $Fe_3C$ → $Fe^{3+}$, respectively.[42]

As we expected, iron-based electrode materials exhibit similar CV behavior with obvious pseudocapacitance feature (Figure 4a), and the potential of charge plateau (Figure S6, Supporting Information) is well agreed with that of the oxidation peak of CV curves. More interestingly, the C-PGF electrode exhibits high specific capacitance of 717 F $g^{-1}$ at a scan rate of 2 mV $s^{-1}$ (Figure 4b), higher than that of C-PF (546 F $g^{-1}$), C-GF (328 F $g^{-1}$) and iron powder (223 F $g^{-1}$) and other $FeO_x$-carbon hybrid materials,[29,30,43] and comparable to or even higher than that of the cathode materials such as $MnO_2$, $Co_3O_4$, $V_2O_5$, $WO_{3-x}$ and $MoO_3$.[8,44−47] Even at high scan rate of 100 mV $s^{-1}$, the capacitance of C-PGF can be up to 413 F $g^{-1}$, much higher than the corresponding value of the other three materials, meaning a good rate performance. Therefore, the ultrahigh specific capacitance may be related with efficient utilization of the active material as a result of the uniform distribution of active material on nitrogen-doped conductive graphene sheets. Moreover, iron nanosheets are directly and selectively grown on the

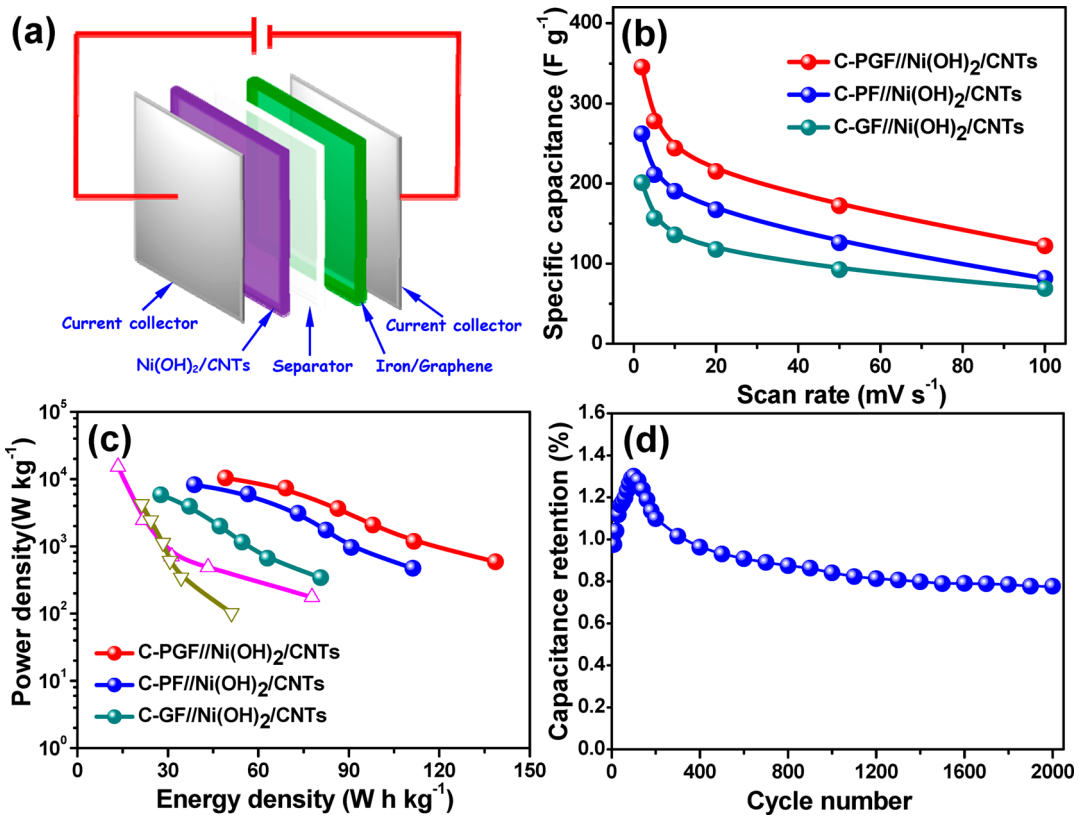


**Figure 5. (a) Schematic illustration of the fabricated asymmetric supercapacitors device based on iron nanocomposite as negative electrode and $Ni(OH)_2$/CNTs as positive electrode in 6 M KOH aqueous electrolyte. (b) The specific capacitance of C-PGF//$Ni(OH)_2$/CNTs, C-PF//$Ni(OH)_2$/CNTs, C-GF//$Ni(OH)_2$/CNTs at different scan rates in 6 M KOH aqueous solution. (c) Ragone plots related to energy and power densities of the as-fabricated supercapacitors and several asymmetric supercapacitors previously reported in the literature, *i.e.*, $Ni(OH)_2$/Graphene//Graphene (△)[7] and $MnO_2$/Graphene//Actived Carbon (▽).[49] (d) Cycle performance of the C-PGF//$Ni(OH)_2$/CNTs at 100 mV $s^{-1}$.**

graphene substrates, resulting in the strong bonding and coupling between iron nanosheets and graphene in the hybrid nanostructures, which significantly enhance the charge transfer for the electrode.

The cycling performance of C-PGF using a three-electrode system is recorded as shown in Figure S7a (Supporting Information). A capacitance increase of *ca.* 20% of the initial capacitance after ~20 cycles is clearly observed, which may result from the gradual activation process of the electroactive iron nanosheets.[12] After that, a decay *ca.* 20% in capacitance is observed after 1000 cycles. This instability could be mainly associated with the aggregation of $Fe_3O_4$ particles through electrochemical cycles, as revealed by TEM images (Figure S7b,c, Supporting Information), resulting in the loss of active material bonding and coupling with the conducting graphene sheets, and subsequent loss of the electrochemical activity.[25]

Although asymmetric supercapacitors have aroused more and more attention and gradually became the hotspot of intense research over the past years,[2,25] reasonable matching of negative/positive electrode is very important for achieving a high energy density for asymmetric supercapacitors due to low capacitance of negative electrode compared to positive electrode. As the negative electrode, the capacitance of C-PGF is much higher than those of porous carbon materials (less than 300 F $g^{-1}$); we expect it to achieve a high energy density for asymmetric supercapacitors.

To further investigate the electrochemical performance of the iron-based electrode materials, two-electrode asymmetric supercapacitors were fabricated and investigated by a two-electrode system (see Experimental Section) using $Ni(OH)_2$/CNTs hybrid material (Figure S8a,b, Supporting Information) as the positive electrode and C-PGF, C-PF or C-GF as the negative electrode with a voltage window of 0−1.7 V in 6 M KOH aqueous electrolyte (Figure 5a). Here, the positive electrode $Ni(OH)_2$/CNTs has a pseudocapacitance characteristic and a high capacitance of 2200 F $g^{-1}$ at 2 mV $s^{-1}$ (Figure S8c,d, Supporting Information), comparable to previous reported values.[48] As a result, the CV curves (Figure S9, Supporting Information) and specific capacitance of as-fabricated asymmetric supercapacitor C-PGF//$Ni(OH)_2$/CNTs (Figure 5b) show high specific capacitance of 345 F $g^{-1}$ at 2 mV $s^{-1}$ and maintain as high as 122 F $g^{-1}$ at 100 mV $s^{-1}$ (corresponding to a full charging or discharging time from 17 s to 14 min), higher than those of C-PF//$Ni(OH)_2$/CNTs (262 F $g^{-1}$ at 2 mV $s^{-1}$ and 82 F $g^{-1}$ at 100 mV $s^{-1}$) and C-GF//$Ni(OH)_2$/CNTs (201 F $g^{-1}$ at

2 mV $s^{-1}$ and 69 F $g^{-1}$ at 100 mV $s^{-1}$). The excellent electrochemical performances of the cell originate from high specific capacitance of negative electrode material, high operating voltage of the asymmetric supercapacitor, as well as good matching of the positive and negative electrodes for electrochemical process.

The energy and power densities calculated for the cells were shown in the Ragone plots (Figure 5c). The C-PGF//$Ni(OH)_2$/CNT asymmetric supercapacitor showed an energy density of 139 Wh $kg^{-1}$ at a power density of 588 W $kg^{-1}$, and a power density of 12.3 kW $kg^{-1}$ at an energy density of 58 Wh $kg^{-1}$, higher than those of other hybrid supercapacitors, such as $MnO_2$/Graphene//AC,[49] $MnO_2$/Graphene//Graphene,[10] $Ni(OH)_2$/Graphene//Graphene,[7] sGNS/cMWCNT/PANI//aGNS,[35] $MnO_2$//polyaniline,[50] $MnO_2$//$Fe_3O_4$,[51] $MnO_2$//FeOOH,[52] and comparable to rechargeable LIBs.[37,53]

The long-term cycling performance of the C-PGF//$Ni(OH)_2$/CNTs asymmetric supercapacitor at a scan rate of 100 mV $s^{-1}$ for 2000 cycles is shown in Figure 5d. A capacitance increase of *ca.* 30% of the initial capacitance after 70 cycles has been observed, which is attributed to the increased effective interfacial area between electrode materials and electrolyte, as well as the full activation of the electrode.[3,22] Moreover, about 78% of the initial capacitance is maintained after 2000 cycles. The capacitance decay may be mainly related with the negative electrode material because of the aggregation $Fe_3O_4$ particles during the charge/discharge process. To improve the cycling stability of negative electrode, the design of active materials with architectures such as nanostructure arrays,[54] synergetic core–shell structures,[55] and hybrid film electrodes[12] is necessary.

## CONCLUSION

In summary, fish scale-like iron nanosheets directly grown on 2D nitrogen-doped carbon substrate are guided by the carbonization of $Fe^{3+}$ adsorbed onto PANI nanosheets/GO composite. The synergistic effect of iron nanosheets and graphene sheets is beneficial for the charge transfer during redox process, resulting in high specific capacitance. More importantly, asymmetric supercapacitors based on iron negative electrode and nickel positive electrode exhibit a noticeable ultrahigh energy density and acceptable cycling performance. Compared to comparable energy density of conventional Ni–Fe batteries, the new asymmetric supercapacitor achieves nearly 1000 times higher power density and approximately 3 times higher energy density, rendering it a high-performance, low cost, safe and environmentally benign energy storage device.

## EXPERIMENTAL SECTION

**Preparation of GO and CNTs.** Graphene oxide (GO) was synthesized from natural graphite (300 $\mu$m, Qingdao Graphite Co., Ltd., China) by a modified Hummers method.[56] Carbon nanotubes (CNTs) were prepared from the decomposition of hydrocarbons over Fe/Mo/$Al_2O_3$ catalyst using a fluidization method. Before use, CNTs were purified and cut in a mixture of concentrated $H_2SO_4$/$HNO_3$ (3:1, v/v) at 100 °C for 2 h.[57]

**Synthesis of Electrode Materials.** Polyaniline (PANI) and polyaniline/graphene oxide (PG) were prepared using *in situ* oxidative polymerization of aniline with (or without) presence of dispersed GO as described elsewhere.[57] The negative materials were synthesized by pyrolysis of the iron-containing mixtures in a tube furnace under $N_2$ atmosphere at 850 °C for 2 h. Briefly, iron nitrate nonahydrate (0.4 g, 1 mM) completely dissolved in ethanol (20 mL), and PG (or PANI or GO) (0.5 g) was added, and then continuous stirring was taken until the ethanol was completely evaporated. After that, the powders were heated to 850 °C and pyrolyzed for 2 h under nitrogen flow, and the as-obtained sample was named as C-PGF, C-PF and C-GF, respectively. For comparison, pure carbon material (C-PG) was synthesized by the same procedure as described above in the absence of iron nitrate. The positive material $Ni(OH)_2$/CNTs was synthesized by a simple hydrothermal method using nickel sulfate hexahydrate, urea as source materials. Typically, nickel sulfate hexahydrate (157.7 mg, 0.6 mM) dissolved in dispersed CNTs (0.167 mg $mL^{-1}$, 30 mL) to form a suspension. After continuously stirring for 1 h, urea (216.2 mg, 3.6 mM) was added into it. After 30 min of stirring, the mixture was poured into a Teflon-lined stainless reactor (40 mL) with the volume filling ration of 75%. Subsequently, the mixture was heated at 170 °C for 18 h and cooled down to room temperature naturally. After that, the products were washed with deionized water and ethanol several times until the pH value remained constant. Finally, they were dried in an oven at 100 °C for 12 h.

**Materials Characterization.** Thermogravimetric (TG) analysis was conducted on a thermogravimetric analyzer Mettler Toledo. The sample was heated up to 900 °C in air with a heating rate of 20 °C $min^{-1}$. The crystallographic structures of the materials were determined by a powder XRD system (TTR-III) equipped with Cu K$\alpha$ radiation ($\lambda$ = 0.15418 nm) at a scanning rate of 10° $min^{-1}$ in the 2$\theta$ range from 5° to 80°. FTIR spectroscopy was carried out on a Perkin-Elmer Spectrum 100 spectrometer in a range of 500–4000 $cm^{-1}$. Raman scattering spectra were obtained on a Jobin-Yvon HR-800 Raman spectrometer with 632.8 nm wavelength incident laser light. The scanning electron microscopy (SEM) images were conducted on a Hitachi S-4800. The transmission electron microscope (TEM) images, high-resolution TEM (HRTEM) and scanning TEM (STEM) images were performed on a FEI Tecnai TF20. $N_2$ sorption analysis was recorded from a Quantachrome autosorb $iQ_2$ instrument, equipped with automated gas absorb analyzer, at 77 K using Barrett–Emmett–Teller (BET) calculations for the surface area. The pore size distribution (PSD) plot was conducted on the adsorption branch of the isotherm based on density functional theory (DFT) model.

**Electrochemical Measurements.** The individual electrodes used for the electrochemical tests were prepared by mixing the active material, carbon black, and polytetrafluoroethylene (PTFE) with ethanol in a mass ratio of 75:20:5 to obtain a slurry. Then the slurry was pressed onto the nickel foam current collector (1 cm × 1 cm) and dried in the oven at 60 °C for 12 h. The electrochemical tests of the individual electrode were performed in a three-electrode cell, in which platinum foil and Hg/HgO (or SCE) electrodes were used as the counter and reference electrodes, respectively. To fabricate asymmetric supercapacitors, the $Ni(OH)_2$/CNTs cathode and C-PGF anode were pressed together and separated by a porous nonwoven cloth separator. The electrochemical measurements of the asymmetric supercapacitors were carried out in a two-electrode cell at room temperature in 6 M KOH aqueous electrolyte solution. All of the above electrochemical measurements were carried out by a CHI 660C electrochemical workstation at ambient temperature.

The specific capacitance of the electrodes or cells can be calculated from the CV curves according to the following equation:[7]

$$C = \frac{\int I\,dV}{\upsilon m V} \quad (1)$$

where $C$ is the specific capacitance (F $g^{-1}$) based on the mass of the active materials, $I$ is the current density (A $cm^{-2}$), $V$ is the potential or cell voltage (V), $\upsilon$ is the scan rate (mV $s^{-1}$), and $m$ is the mass of the active materials of individual electrode or the total mass of active materials on the two electrodes of the as-assembled capacitor (g $cm^{-2}$).

The optimal mass ratio between the two electrodes can be expressed as follows:[58]

$$\frac{m_+}{m_-} = \frac{C_- \times V_-}{C_+ \times V_+} \quad (2)$$

where $m$ (g) is the mass of electrode, $C$ (F $g^{-1}$) is the specific capacitance of electrode based on eq 1, $V$ (V) is the working potential of the electrode.

The key parameters of the supercapacitor, power density ($P$) and energy density ($E$), were calculated using eqs 3 and 4:

$$E = \frac{1}{2}CV^2 \quad (3)$$

$$P = \frac{E}{\Delta t} \quad (4)$$

where $C$ (F $g^{-1}$) represents the specific capacitance of the supercapacitor measured from the eq 1, $V$ (V) refers to the potential change within the discharge time $\Delta t$ (s), $E$ (J $g^{-1}$) is the energy density, and $P$ (W $g^{-1}$) is the power density.

*Conflict of Interest:* The authors declare no competing financial interest.

*Acknowledgment.* The authors acknowledge financial support from the National Science Foundation of China (51077014, 21003028 and 51202043), Fundamental Research funds for the Central Universities, Program for New Century Excellent Talents in University (NCET-10-0050), and Excellent Youth Foundation of Heilongjiang Province of China.

*Supporting Information Available:* FTIR spectra of PG, Raman spectra of C-PGF, the adsorption isotherm of PG, the XRD pattern of samples, TG curve of C-PGF, TEM images of samples, the galvanostatic charge curves of C-PGF, the CV curves and specific capacitance of samples. This material is available free of charge *via* the Internet at http://pubs.acs.org.

## REFERENCES AND NOTES

1. Jiang, J.; Li, Y.; Liu, J.; Huang, X.; Yuan, C.; Lou, X. W. Recent Advances in Metal Oxide-Based Electrode Architecture Design for Electrochemical Energy Storage. *Adv. Mater.* **2012**, *24*, 5166–5180.
2. Chen, Z.; Wen, J.; Yan, C.; Rice, L.; Sohn, H.; Shen, M.; Cai, M.; Dunn, B.; Lu, Y. High-Performance Supercapacitors Based on Hierarchically Porous Graphite Particles. *Adv. Energy Mater.* **2011**, *1*, 551–556.
3. Yuan, C.; Li, J.; Hou, L.; Zhang, X.; Shen, L.; Lou, X. W. D. Ultrathin Mesoporous $NiCo_2O_4$ Nanosheets Supported on Ni Foam as Advanced Electrodes for Supercapacitors. *Adv. Funct. Mater.* **2012**, *22*, 4592–4597.
4. Liu, C.; Li, F.; Ma, L. P.; Cheng, H. M. Advanced Materials for Energy Storage. *Adv. Energy Mater.* **2010**, *22*, E28–62.
5. Zhang, G.; Lou, X. W. General Solution Growth of Mesoporous $NiCo_2O_4$ Nanosheets on Various Conductive Substrates as High-Performance Electrodes for Supercapacitors. *Adv. Mater.* **2013**, *25*, 976–979.
6. Izadi-Najafabadi, A.; Yasuda, S.; Kobashi, K.; Yamada, T.; Futaba, D. N.; Hatori, H.; Yumura, M.; Iijima, S.; Hata, K. Extracting the Full Potential of Single-Walled Carbon Nanotubes as Durable Supercapacitor Electrodes Operable at 4 V with High Power and Energy Density. *Adv. Energy Mater.* **2010**, *22*, E235–241.
7. Yan, J.; Fan, Z.; Sun, W.; Ning, G.; Wei, T.; Zhang, Q.; Zhang, R.; Zhi, L.; Wei, F. Advanced Asymmetric Supercapacitors Based on $Ni(OH)_2$/Graphene and Porous Graphene Electrodes with High Energy Density. *Adv. Funct. Mater.* **2012**, *22*, 2632–2641.
8. Chen, Z.; Augustyn, V.; Wen, J.; Zhang, Y.; Shen, M.; Dunn, B.; Lu, Y. High-Performance Supercapacitors Based on Intertwined CNT/$V_2O_5$ Nanowire Nanocomposites. *Adv. Mater.* **2011**, *23*, 791–795.
9. Chen, P.-C.; Shen, G.; Shi, Y.; Chen, H.; Zhou, C. Preparation and Characterization of Flexible Asymmetric Supercapacitors Based on Transition-Metal-Oxide Nanowire/Single-Walled Carbon Nanotube Hybrid Thin-Film Electrodes. *ACS Nano* **2010**, *4*, 4403–4411.
10. Wu, Z.-S.; Ren, W.; Wang, D.-W.; Li, F.; Liu, B.; Cheng, H.-M. High-Energy $MnO_2$ Nanowire/Graphene and Graphene Asymmetric Electrochemical Capacitors. *ACS Nano* **2010**, *4*, 5835–5842.
11. Chen, W.; Rakhi, R. B.; Hu, L.; Xie, X.; Cui, Y.; Alshareef, H. N. High-Performance Nanostructured Supercapacitors on a Sponge. *Nano Lett.* **2011**, *11*, 5165–5172.
12. Zhang, F.; Yuan, C.; Zhu, J.; Wang, J.; Zhang, X.; Lou, X. W. D. Flexible Films Derived from Electrospun Carbon Nanofibers Incorporated with $Co_3O_4$ Hollow Nanoparticles as Self-Supported Electrodes for Electrochemical Capacitors. *Adv. Funct. Mater.* **2013**, *23*, 3909–3915.
13. Lou, X. W.; Deng, D.; Lee, J. Y.; Feng, J.; Archer, L. A. Self-Supported Formation of Needlelike $Co_3O_4$ Nanotubes and Their Application as Lithium-Ion Battery Electrodes. *Adv. Mater.* **2008**, *20*, 258–262.
14. Yang, S.; Wu, X.; Chen, C.; Dong, H.; Hu, W.; Wang, X. Spherical alpha-$Ni(OH)_2$ Nanoarchitecture Grown on Graphene as Advanced Electrochemical Pseudocapacitor Materials. *Chem. Commun.* **2012**, *48*, 2773–2775.
15. Wang, Y. G.; Li, H. Q.; Xia, Y. Y. Ordered Whiskerlike Polyaniline Grown on the Surface of Mesoporous Carbon and Its Electrochemical Capacitance Performance. *Adv. Mater.* **2006**, *18*, 2619–2623.
16. Li, Z.; Zhang, L.; Amirkhiz, B. S.; Tan, X.; Xu, Z.; Wang, H.; Olsen, B. C.; Holt, C. M. B.; Mitlin, D. Carbonized Chicken Eggshell Membranes with 3D Architectures as High-Performance Electrode Materials for Supercapacitors. *Adv. Energy Mater.* **2012**, *2*, 431–437.
17. Lee, J.; Kim, J.; Hyeon, T. Recent Progress in the Synthesis of Porous Carbon Materials. *Adv. Mater.* **2006**, *18*, 2073–2094.
18. Li, L. X.; Song, H. H.; Chen, X. H. Pore Characteristics and Electrochemical Performance of Ordered Mesoporous Carbons for Electric Double-Layer Capacitors. *Electrochim. Acta* **2006**, *51*, 5715–5720.
19. Wang, Q.; Yan, J.; Wang, Y.; Ning, G.; Fan, Z.; Wei, T.; Cheng, J.; Zhang, M.; Jing, X. Template Synthesis of Hollow Carbon Spheres Anchored on Carbon Nanotubes for High Rate Performance Supercapacitors. *Carbon* **2013**, *52*, 209–218.
20. Yang, M.; Cheng, B.; Song, H.; Chen, X. Preparation and Electrochemical Performance of Polyaniline-Based Carbon Nanotubes as Electrode Material for Supercapacitor. *Electrochim. Acta* **2010**, *55*, 7021–7027.
21. Huang, Y.; Liang, J.; Chen, Y. An Overview of the Applications of Graphene-Based Materials in Supercapacitors. *Small* **2012**, *8*, 1805–1834.
22. Fan, Z.; Yan, J.; Zhi, L.; Zhang, Q.; Wei, T.; Feng, J.; Zhang, M.; Qian, W.; Wei, F. A Three-Dimensional Carbon Nanotube/Graphene Sandwich and Its Application as Electrode in Supercapacitors. *Adv. Mater.* **2010**, *22*, 3723–3728.
23. Fang, Y.; Luo, B.; Jia, Y.; Li, X.; Wang, B.; Song, Q.; Kang, F.; Zhi, L. Renewing Functionalized Graphene as Electrodes for High-Performance Supercapacitors. *Adv. Mater.* **2012**, *24*, 6348–6355.
24. Hao, L.; Li, X.; Zhi, L. Carbonaceous Electrode Materials for Supercapacitors. *Adv. Mater.* **2013**, *25*, 3899–3904.
25. Wang, H.; Liang, Y.; Gong, M.; Li, Y.; Chang, W.; Mefford, T.; Zhou, J.; Wang, J.; Regier, T.; Wei, F.; Dai, H. An Ultrafast Nickel-Iron Battery from Strongly Coupled Inorganic

Nanoparticle/Nanocarbon Hybrid Materials. *Nat. Commun.* **2012**, *3*, 917–924.
26. Qu, Q.; Yang, S.; Feng, X. 2D Sandwich-Like Sheets of Iron Oxide Grown on Graphene as High Energy Anode Material for Supercapacitors. *Adv. Mater.* **2011**, *23*, 5574–5580.
27. Wang, L.; Ji, H.; Wang, S.; Kong, L.; Jiang, X.; Yang, G. Preparation of $Fe_3O_4$ with High Specific Surface Area and Improved Capacitance as a Supercapacitor. *Nanoscale* **2013**, *5*, 3793–3799.
28. Ji, L.; Toprakci, O.; Alcoutlabi, M.; Yao, Y.; Li, Y.; Zhang, S.; Guo, B.; Lin, Z.; Zhang, X. Alpha-$Fe_2O_3$ Nanoparticle-Loaded Carbon Nanofibers as Stable and High-Capacity Anodes for Rechargeable Lithium-Ion Batteries. *ACS Appl. Mater. Interfaces* **2012**, *4*, 2672–2679.
29. Liu, D.; Wang, X.; Wang, X.; Tian, W.; Liu, J.; Zhi, C.; He, D.; Bando, Y.; Golberg, D. Ultrathin Nanoporous $Fe_3O_4$-Carbon Nanosheets with Enhanced Supercapacitor Performance. *J. Mater. Chem. A* **2013**, *1*, 1952–1955.
30. Xia, X.; Hao, Q.; Lei, W.; Wang, W.; Sun, D.; Wang, X. Nanostructured Ternary Composites of Graphene/$Fe_2O_3$/Polyaniline for High-Performance Supercapacitors. *J. Mater. Chem.* **2012**, *22*, 16844–16850.
31. Liu, Z.; Tay, S. W.; Li, X. Rechargeable Battery Using a Novel Iron Oxide Nanorods Anode and a Nickel Hydroxide Cathode in an Aqueous Electrolyte. *Chem. Commun.* **2011**, *47*, 12473–12475.
32. Tang, Z.; Tang, C.-h.; Gong, H. A High Energy Density Asymmetric Supercapacitor from Nano-Architectured Ni-$(OH)_2$/Carbon Nanotube Electrodes. *Adv. Funct. Mater.* **2012**, *22*, 1272–1278.
33. Lu, X.; Yu, M.; Wang, G.; Zhai, T.; Xie, S.; Ling, Y.; Tong, Y.; Li, Y. H-$TiO_2$@$MnO_2$//H-$TiO_2$@C Core-Shell Nanowires for High Performance and Flexible Asymmetric Supercapacitors. *Adv. Mater.* **2013**, *25*, 267–272.
34. Sumboja, A.; Foo, C. Y.; Wang, X.; Lee, P. S. Large Areal Mass, Flexible and Free-Standing Reduced Graphene Oxide/Manganese Dioxide Paper for Asymmetric Supercapacitor Device. *Adv. Mater.* **2013**, *25*, 2809–2815.
35. Shen, J.; Yang, C.; Li, X.; Wang, G. High-Performance Asymmetric Supercapacitor Based on Nanoarchitectured Polyaniline/Graphene/Carbon Nanotube and Activated Graphene Electrodes. *ACS Appl. Mater. Interfaces* **2013**, *5*, 8467–8476.
36. Thackeray, M. M.; Wolverton, C.; Isaacs, E. D. Electrical Energy Storage for Transportation-Approaching the Limits of, and Going Beyond, Lithium-Ion Batteries. *Energy Environ. Sci.* **2012**, *5*, 7854–7863.
37. Jeong, G.; Kim, Y.-U.; Kim, H.; Kim, Y.-J.; Sohn, H.-J. Prospective Materials and Applications for Li Secondary Batteries. *Energy Environ. Sci.* **2011**, *4*, 1986–2002.
38. Wang, J.; Deng, B.; Chen, H.; Wang, X.; Zheng, J. Removal of Aqueous Hg(II) by Polyaniline: Sorption Characteristics and Mechanisms. *Environ. Sci. Technol.* **2009**, *43*, 5223–5228.
39. Zhu, Y.; Murali, S.; Cai, W.; Li, X.; Suk, J. W.; Potts, J. R.; Ruoff, R. S. Graphene and Graphene Oxide: Synthesis, Properties, and Applications. *Adv. Mater.* **2010**, *22*, 3906–3924.
40. Prakash, R.; Mishra, A. K.; Roth, A.; Kübel, C.; Scherer, T.; Ghafari, M.; Hahn, H.; Fichtner, M. A Ferrocene-Based Carbon-Iron Lithium Fluoride Nanocomposite as a Stable Electrode Material in Lithium Batteries. *J. Mater. Chem.* **2010**, *20*, 1871–1876.
41. Zhao, M.; Song, H. Synthesis of Carbon-Encapsulated Iron Carbide/Iron Nanoparticles from Phenolic-Formaldehyde Resin and Ferric Nitrate. *Mater. Chem. Phys.* **2010**, *124*, 861–864.
42. Ujimine, K.; Tsutsumi, A. Electrochemical Characteristics of Iron Carbide as an Active Material in Alkaline Batteries. *J. Power Sources* **2006**, *160*, 1431–1435.
43. Shi, W.; Zhu, J.; Sim, D. H.; Tay, Y. Y.; Lu, Z.; Zhang, X.; Sharma, Y.; Srinivasan, M.; Zhang, H.; Hng, H. H.; Yan, Q. Achieving High Specific Charge Capacitances in $Fe_3O_4$/Reduced Graphene Oxide Nanocomposites. *J. Mater. Chem.* **2011**, *21*, 3422–3427.
44. Yu, Z.; Duong, B.; Abbitt, D.; Thomas, J. Highly Ordered $MnO_2$ Nanopillars for Enhanced Supercapacitor Performance. *Adv. Mater.* **2013**, *25*, 3302–3306.
45. Xiao, Y.; Liu, S.; Li, F.; Zhang, A.; Zhao, J.; Fang, S.; Jia, D. 3D Hierarchical $Co_3O_4$ Twin-Spheres with an Urchin-Like Structure: Large-Scale Synthesis, Multistep-Splitting Growth, and Electrochemical Pseudocapacitors. *Adv. Funct. Mater.* **2012**, *22*, 4052–4059.
46. Chang, K.-H.; Hu, C.-C.; Huang, C.-M.; Liu, Y.-L.; Chang, C.-I. Microwave-Assisted Hydrothermal Synthesis of Crystalline $WO_3$-$WO_3 \cdot 0.5H_2O$ Mixtures for Pseudocapacitors of the Asymmetric Type. *J. Power Sources* **2011**, *196*, 2387–2392.
47. Brezesinski, T.; Wang, J.; Tolbert, S. H.; Dunn, B. Ordered Mesoporous alpha-$MoO_3$ with Iso-Oriented Nanocrystalline Walls for Thin-Film Pseudocapacitors. *Nat. Mater.* **2010**, *9*, 146–151.
48. Yan, J.; Sun, W.; Wei, T.; Zhang, Q.; Fan, Z.; Wei, F. Fabrication and Electrochemical Performances of Hierarchical Porous Ni$(OH)_2$ Nanoflakes Anchored on Graphene Sheets. *J. Mater. Chem.* **2012**, *22*, 11494–11502.
49. Fan, Z.; Yan, J.; Wei, T.; Zhi, L.; Ning, G.; Li, T.; Wei, F. Asymmetric Supercapacitors Based on Graphene/$MnO_2$ and Activated Carbon Nanofiber Electrodes with High Power and Energy Density. *Adv. Funct. Mater.* **2011**, *21*, 2366–2375.
50. Khomenko, V.; Raymundo-Piñero, E.; Frackowiak, E.; Béguin, F. High-Voltage Asymmetric Supercapacitors Operating in Aqueous Electrolyte. *Appl. Phys. A: Mater. Sci. Process.* **2005**, *82*, 567–573.
51. Cottineau, T.; Toupin, M.; Delahaye, T.; Brousse, T.; Bélanger, D. Nanostructured Transition Metal Oxides for Aqueous Hybrid Electrochemical Supercapacitors. *Appl. Phys. A: Mater. Sci. Process.* **2005**, *82*, 599–606.
52. Jin, W.-H.; Cao, G.-T.; Sun, J.-Y. Hybrid Supercapacitor Based on $MnO_2$ and Columned FeOOH Using $Li_2SO_4$ Electrolyte Solution. *J. Power Sources* **2008**, *175*, 686–691.
53. Guo, S.; Dong, S. Graphene Nanosheet: Synthesis, Molecular Engineering, Thin Film, Hybrids, and Energy and Analytical Applications. *Chem. Soc. Rev.* **2011**, *40*, 2644–2672.
54. Zhang, G. Q.; Wu, H. B.; Hoster, H. E.; Chan-Park, M. B.; Lou, X. W. Single-Crystalline $NiCo_2O_4$ Nanoneedle Arrays Grown on Conductive Substrates as Binder-Free Electrodes for High-Performance Supercapacitors. *Energy Environ. Sci.* **2012**, *5*, 9453–9456.
55. Yu, L.; Zhang, G.; Yuan, C.; Lou, X. W. Hierarchical $NiCo_2O_4$@$MnO_2$ Core-Shell Heterostructured Nanowire Arrays on Ni Foam as High-Performance Supercapacitor Electrodes. *Chem. Commun.* **2013**, *49*, 137–139.
56. Hummers, W. S.; Offeman, R. E. Preparation of Graphitic Oxide. *J. Am. Chem. Soc.* **1958**, *80*, 1339.
57. Ning, G.; Li, T.; Yan, J.; Xu, C.; Wei, T.; Fan, Z. Three-Dimensional Hybrid Materials of Fish Scale-Like Polyaniline Nanosheet Arrays on Graphene Oxide and Carbon Nanotube for High-Performance Ultracapacitors. *Carbon* **2013**, *54*, 241–248.
58. Khomenko, V.; Raymundo-Piñero, E.; Béguin, F. Optimisation of an Asymmetric Manganese Oxide/Activated Carbon Capacitor Working at 2 V in Aqueous Medium. *J. Power Sources* **2006**, *153*, 183–190.